Generation of Hypothetical Radiances for Missing Green and Red Bands in Geostationary Environment Monitoring Spectrometer

Han-Sol Ryu, Jeong-Eun Park, Jaehoon Jeong, and Sungwook Hong

***Abstract*—True-color imagery is essential for an intuitive comprehension of atmospheric data. However, the Geostationary Environment Monitoring Spectrometer (GEMS) of the geostationary Korea multipurpose satellite (GK) 2B lacks green and red bands, which limits its ability to monitor atmospheric environments. To mitigate this issue, we suggest an innovative method of generating virtual GEMS green and red bands using conditional generative adversarial networks with data observed in the blue-green-red (RGB) bands of the Advanced Meteorological Imager sensor, a payload of the GK-2A satellite. The paired datasets of the AMI blue band and the AMI RGB bands were used to train and test the data-to-data (D2D) translation model. Using the GEMS blue band as input data, the D2D model generated GEMS hypothetical radiance data at the green and red bands. Our results show that the D2D model generated hypothetical GEMS green and red bands with outstanding performance. The averaged values of the correlation coefficient, root-mean-square error, and bias between the observed and D2D-generated GEMS blue band were 0.999, 3.450 W/cm^2/cm/sr, and −1.858 W/cm^2/cm/sr, respectively. This research is expected to significantly contribute to the monitoring and comprehension of atmospheric environments in Asia and potentially improve the GEMS's global ability to monitor air quality. Additionally, the proposed method has the potential to enhance the capabilities of other satellites with limited spectral bands.**

***Index Terms*—Advanced meteorological imager (AMI), data-to-data translation, geostationary environment monitoring spectrometer (GEMS), hypothetical blue-green-red (RGB), satellite remote sensing.**

Manuscript received 4 April 2023; revised 22 May 2023; accepted 24 May 2023. Date of publication 29 May 2023; date of current version 5 October 2023. This work was supported in part by a grant from the National Institute of Environment Research, funded by the Ministry of Environment of the Republic of Korea under Grant NIER-2021-01-01-052, Grant NIER-2022-01-02-096, and Grant NIER-2023-01-02-095, and in part by "Development of Advanced Science and Technology for Marine Environmental Impact Assessment" of Korea Institute of Marine Science and Technology Promotion (KIMST) funded by the Ministry of Oceans and Fisheries under Grant KIMST-20210427. *(Corresponding author: Sungwook Hong.)*

Han-Sol Ryu and Jeong-Eun Park are with the Department of Environment, Energy, and Geoinfomatics, Sejong University, Gwangjin-gu 05006, South Korea (e-mail: hansol@sju.ac.kr; wjd196@sju.ac.kr).

Jaehoon Jeong is with the National Institute of Environmental Research, Seogu 22678, South Korea (e-mail: jaehoon80@korea.kr).

Sungwook Hong is with the Department of Environment, Energy, and Geoinfomatics, Sejong University, Gwangjin-gu 05006, South Korea, and also with the DeepThoTh Company, Ltd., Gwangjin-gu 05006, South Korea (e-mail: sesttiya@sejong.ac.kr).

Digital Object Identifier 10.1109/JSTARS.2023.3280905

I. Introduction

Air pollution is a global issue for the atmospheric environment owing to its detrimental effects on public health [1], [2], [3]. Recently, Asia, which contains half of the global population, has experienced high levels of air pollution. Atmospheric pollution gases include aerosols, ozone (O_3), nitrogen dioxide (NO_2), sulfur dioxide (SO_2), carbon monoxide (CO), particulate matter ($PM_{2.5}$ and PM_{10}), and formaldehyde (HCHO) [3].

Satellites are currently the only tools capable of quantitatively monitoring global air quality, including pollutant quantities, emissions, and transportation [4]. Since the late 1970s, aerosols and numerous atmospheric pollution gases have been observed and monitored using a variety of sensors mounted on satellites, including the Global Ozone Monitoring Experiments 1 and 2 [5], [6], [7], the moderate resolution imaging spectroradiometer [8], the ozone mapping profiler suite [9], the Ozone Monitoring Instrument (OMI) [4], the scanning imaging absorption spectrometer for atmospheric cartography [10], the Solar Backscatter Ultraviolet Radiometer [11], the Total Ozone Mapping Spectrometer (TOMS) [11], the tropospheric monitoring instrument (TROPOMI) [12], and the visible infrared imaging radiometer suite [13].

The geostationary Korea multipurpose satellite (GK) 2A satellite carrying the Advanced Meteorological Imager (AMI) was launched for meteorological purposes in Dec. 2018. In Feb. 2020, the GK-2B satellite equipped with a Geostationary Ocean Color Imager (GOCI) 2 and Geostationary Environment Monitoring Spectrometer (GEMS) was launched for ocean color and environmental monitoring purposes [14], [15].

GEMS provides Level 2 products such as aerosols, clouds, O_3, NO_2, SO_2, HCHO, surface reflectivity, and ultraviolet (UV) index (UVI). Notably, the GEMS has 1000 bands between 300 and 500 nm with a full width at a half-maximum of 0.6 nm. The spatial resolutions of the GEMS over Seoul, South Korea, are 7 km × 8 km for gases and 3.5 km × 8 km for aerosols, respectively [3], [16]. The GEMS aerosol products were estimated using the OMI aerosol algorithm and an optical estimation method [17], [18], [19], [20], and the Lambertian cloud model forms the basis of the GEMS cloud products [21]. The GEMS O_3 retrieval algorithm implements the TOMS version 9 algorithm [22], [23]. The GEMS NO_2 products were retrieved using a differential optical absorption spectroscopy (DOAS) algorithm that fits spectral optical NO_2 depths in the 432–450 nm range

[24], [25]. The GEMS SO_2 products were retrieved using the principal component analysis and DOAS techniques [26]. The GEMS HCHO products were estimated using a nonlinear direct fitting method in the 328.5–356.5 nm and 435–461 nm ranges [15], [27], [28], [29]. The GEMS surface reflectivity products include the geometry-dependent Lambertian equivalent reflectivity and daily bidirectional reflectance distribution function [30]. The GEMS UVI products were produced using radiative transfer modeling [31].

Recent attention has been drawn to various research fields that combine machine learning (ML) and deep learning (DL) with large amounts of data. The evolution of graphics processing units (GPU) has increased computing power and eliminated numerous limitations in the application of artificial neural networks (ANNs) [32]. The exponential expansion of digital data has opened up significant opportunities and transformational potential in numerous scientific disciplines that rely on data-driven research [33]. The ML and DL techniques have proven to be effective in analyzing satellite data by a multiple researches [34].

Advanced DL techniques, including convolutional long short-term memory [35], convolutional neural networks (CNNs) [36], [37], generative adversarial networks (GANs), and conditional GAN (CGAN) [38], [39], [40], [41], [42], [43], [44], have been utilized in a number of satellite remote sensing researches [45], [46], [47], [48]. These techniques have exhibited beneficial results in overcoming the limitations of conventional approaches relying on satellite observations.

Numerous researches have used ML and DL techniques in conjunction with Korean geostationary satellites to examine the atmospheric environment in Far East Asia. The $PM_{2.5}$ and PM_{10} over South Korea utilizing a random forest (RF) ML-based model were estimated using combined data with model-based meteorological parameters, emission parameters, and satellite-derived aerosol optical depth (AOD) [49]. The ANN method was used to recalibrate the erroneous pixels in the GEMS data [50]. The spatiotemporal properties of the hourly AOD over Northeast Asia observed by the GOCI sensor were estimated using a physical model, ML-based models (RF and support vector regression methods), and a deep neural network model [51].

True-color imagery captured by a satellite's blue-green-red (RGB) bands can provide both expert and general users with diverse atmospheric and surface information due to their visualization, intuitive understanding, and minimal loss of observational data [52]. Notably, GEMS has only one blue band in the visible (VIS) wavelength range because of its narrow light spectrum range [53].

AMI, GEMS, and GOCI-2 sensors sharing the satellite locations provide advantages and disadvantages regarding synergistic effects. The AMI VIS and infrared (IR) bands and the GOCI-2 VIS bands aid in cloud detection. Notably, the relatively higher spatial resolutions of VIS bands in both GOCI-2 (0.25 km) and AMI (0.5–1 km) are advantageous for detecting small-scale cloud contamination [54]. In contrast to AMI and GOCI-2, GEMS lacks VIS bands beyond 500 nm and has a coarser spatial resolution in VIS bands [14].

A few researches have utilized DL techniques to generate synthetic RGB bands through image-to-image translation for satellites, compensating for the absence of specific components within the RGB bands. For instance, one research used CGAN and CNN to create virtual green bands in an Advanced Baseline Imager (ABI) by leveraging the Advanced Himawari Imager (AHI) RGB bands [48]. Another research employed the CGAN method to generate hypothetical RGB bands during daytime and nighttime by using a combination of AMI RGB bands and IR bands [55].

The precise detection of clouds plays a crucial role in conducting accurate atmospheric environmental research and generating secondary products from environmental satellites like GK-2B with GEMS. Currently, GEMS heavily relies on cloud information derived from AMI cloud products, which introduces a time lag. Therefore, this study was motivated to provide real-time GEMS cloud information, enhance the accuracy of GEMS secondary products, and reduce the dependence on AMI data by using the observed GEMS blue band and virtual GEMS green and red bands.

This research aims to present a DL technique utilizing data-to-data (D2D) translation for generating virtual radiances of GEMS green and red bands using the observed radiance at GEMS blue band. The CGAN technique was adopted in this research, using Pix2Pix software [56], to generate the GEMS hypothetical green and red bands. Paired datasets of AMI blue band and AMI RGB bands were utilized to train and test the D2D model, based on the hypothesis that the D2D model trained with AMI data could be applied to the GEMS data, given the identical central wavelength of 470 nm. The D2D-generated GEMS green and red bands could enhance GEMS applications in environmental and atmospheric research and provide valuable support for operational forecasters and analysts.

II. Data and Research Area

This research used the original Level 1 datasets observed from the GEMS blue band and AMI RGB bands. The data from AMI and GEMS were obtained through the National Meteorological Satellite Center of the Korea Meteorological Administration and the National Environmental Satellite Center of Korea's Ministry of Environment.

The AMI and GEMS sensors are located at a longitude of 128.2 °E and 128.0° above the earth's equator, respectively, with distinct spectral response functions (SRF), bandwidths, spatiotemporal resolutions, and scanning modes. The blue (470 nm) band of GEMS has a spatial resolution of 3.5 km×8 km, while the AMI has spatial resolutions of 1 km×1 km in the blue (470 nm) and green (510 nm) bands, and 0.5 km×0.5 km in the red (640 nm) band. The GEMS observes the coverage within the latitudes −6.128°S to 51.187°N and longitudes 49.174°E to 133.306°E, covering most of Asia. For Far-East Asia, the AMI observes the area between latitudes 11.304°N and 61.935°N and longitudes 76.801°E and 175.199°E. The spectral band characteristics of the AMI and GEMS are summarized in Table I. In this study, the GEMS data were collocated and adjusted with

TABLE I
SPECTRAL BAND CHARACTERISTICS OF THE AMI AND GEMS

Features	AMI	GEMS
Wavelength	470 to 1330 (nm)	300 to 500 (nm)
Spatial Resolution	0.5 km × 0.5 km (Red) 1 km × 1 km (VIS) 2 km × 2 km (IR)	7 km × 8 km (Gas) 3.5 km × 8 km (Aerosol)
Spectral Resolution	37–1038 (nm)	0.6 (nm)
Temporal Resolution	10 min (FD, EA)	1 h
Band Numbers	16	1000 (Hyperspectral)
Coverage	Full Disk (FD), Northern Hemisphere FD (NHFD), North-East Asia, Korean Peninsula (LA)	

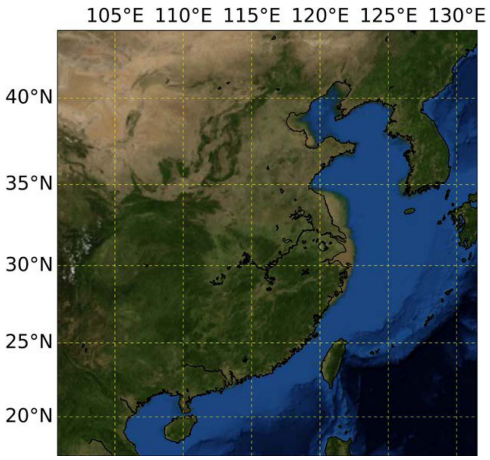

Fig. 1. Study area including parts of Japan, China, and the Korean peninsula.

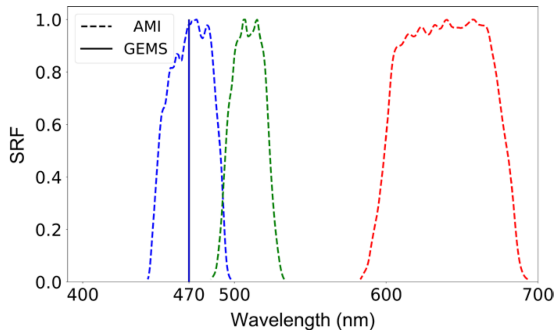

Fig. 2. SRFs of the GEMS blue band and the AMI RGB bands.

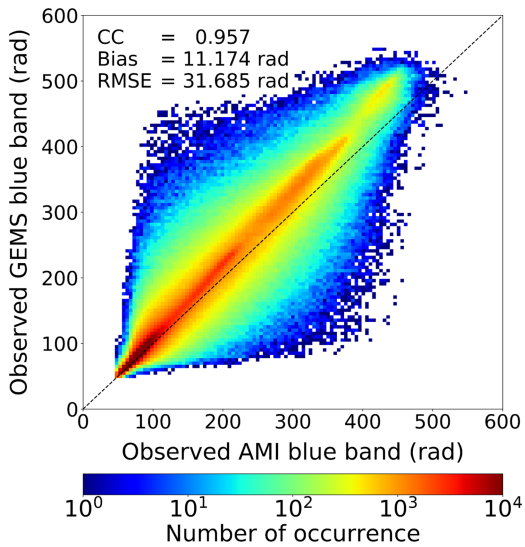

Fig. 3. Scatterplot between the AMI blue band at 03:40 UTC and the GEMS blue band at 03:45 UTC on Jan. 1, 2021. The term "rad" indicates radiance, measured in in W/cm^2/cm/sr units.

an effective spatial resolution of 2 km, identical to the AMI data, using the nearest interpolation method.

Fig. 1 shows the study area defined as the far-east region between 17.15°N to 44°N latitudes and 100°E to 131.7°E longitudes, which includes parts of Japan, China, and the Korean Peninsula.

In this research, the D2D model was constructed using the AMI blue band radiance data in units of "rad" (= W/cm^2/cm/sr) as input and the AMI RGB bands radiance data as output. The GEMS blue band radiance data, which has a central wavelength of 470 nm identical to that of the AMI blue band, was applied to the constructed D2D model.

Fig. 2 shows the SRFs of the AMI RGB bands (dotted lines) and the GEMS blue band (solid line). Notably, the two sensors had identical central wavelengths of the blue band (470 nm) with different spectral resolution (see Table I).

The D2D model must have the same two-dimensional size arrangement [56]. Therefore, to ensure spatial consistency between the GEMS and AMI data, the original GEMS data, which had a different spatial resolution than the AMI data, was preprocessed using a nearest-neighbor interpolation technique.

Fig. 3 shows the scatterplot of the AMI and GEMS blue band (470 nm) with correlation coefficient (CC) = 0.957, root-mean-square error (RMSE) = 31.685 rad, and bias = 11.174 rad on Jan. 1, 2021. In this case, the AMI was observed at 03:40 UTC, while the GEMS was performed at 03:45 UTC with a 5-min time difference. Particularly, the AMI has a wide bandwidth of 75 nm for the blue band, while the GEMS has a narrow bandwidth of 0.6 nm at maximum for the blue band. This difference can lead to a variation in the radiance ranges observed by the two sensors.

III. METHODS

A. Pre- and Postprocessing of Datasets for D2D Translation

The D2D model employed in this research comprises both preprocessing and postprocessing steps. In the preprocessing step, the paired original input datasets were transformed to ensure compatibility with the Pix2Pix software [57]. Meanwhile, in the postprocessing step, the range of the virtual output datasets were adjusted to conform to that of the original datasets.

In this research, pairs of the AMI input datasets, represented as (X_O, Y_O), were used to train and test the D2D model

$$X_O = x_i \in \{\mathrm{AMI}_{O,\,\mathrm{Blue}}\} \tag{1}$$

$$Y_O = y_i \in \{\mathrm{AMI}_{O,\,\mathrm{RGB}}\} \tag{2}$$

where the radiance data observed in the AMI is denoted as AMI_O. Subscripts Blue and RGB indicate the radiance data of the AMI blue band and RGB bands, respectively.

To preprocess the datasets, the radiance values of all the RGB bands of the AMI were converted to normalized numerical values ranging from 0 to 1. The minimum and maximum radiance values of each band were used to normalize the data, and the equation is expressed as follows:

$$R_n = \frac{R_O - R_{\min}}{R_{\max} - R_{\min}} \tag{3}$$

where the notation R denotes the radiance data. The subscripts n, O, max, and min represent normalized data, observed data (X_O or Y_O), and each band's maximum and minimum radiance values, respectively.

After training the D2D model, the virtual normalized AMI RGB data (Y'_V) were generated as output datasets with a numerical array form of size (1850 × 1900 × 3) and ranging from 0 to 1

$$Y_V = Y_{\min} + Y'_V \times (Y_{\max} - Y_{\min}). \tag{4}$$

Finally, the virtual normalized AMI RGB data (Y'_V) were denormalized into the D2D-generated output dataset ($Y_V = Y_{V,\mathrm{RGB}}$) in the range of the original datasets as follows: where $Y_{\max}$ and $Y_{\min}$ denote the corresponding band's maximum and minimum radiance values, respectively.

B. D2D Model Using Pix2Pix Software

For the D2D translation conducted in this research, we employed the Pix2Pix software [57] along with the paired and normalized input datasets. The Pix2Pix software is equipped with the CGAN method, which is derived from the GANs. Like the GANs, the CGAN also comprises two adversarial models, i.e., the generator (G) and the discriminator (D). The generator is a mathematical function that models the distribution of the input numerical array (Y'_O) and generates a corresponding virtual output numerical array (Y'_V). On the other hand, the discriminator is a function that scales and evaluates the probability of the synthesized output data, obtained from the input numerical arrays, belonging to the same distribution as the input numerical array [56], [58].

The Pix2Pix employed a loss function (L_{D2D}) and a combination of adversarial loss (L_a) and reconstruction loss (L_1), as demonstrated below [56]

$$L_{\mathrm{D2D}} = \min_G \max_D \{L_a\} + \lambda \cdot L_1 \tag{5}$$

where $\min_G \max_D \{\}$ indicates the minimum-maximum function between G and D. λ is a factor that explains the balance between adversarial loss (L_a) and reconstruction loss (L_1). This research assigned a value of 1 to λ.

The adversarial loss (L_a) is expressed as follows [56], [58], [59], [60]:

$$L_a = E\left[\log\left(1 - D\left(Y'_O, Y'_V\right)\right)\right] + E\left[\log\left(D\left(Y'_O, Y'_V\right)\right)\right] \tag{6}$$

where Y'_O denote the normalized output data. Y'_V is the virtual output normalized data, expressed as $G(X'_O, Y'_O)$. The log functions in the cross-entropies (E) were introduced to solve the gradient insufficiency problem during the early stage of model training [60]. The first cross-entropy loss function is utilized by the discriminator model to maximize the probability of accurately distinguishing between the observed and generated output data, while the generator model minimizes the second cross-entropy loss function.

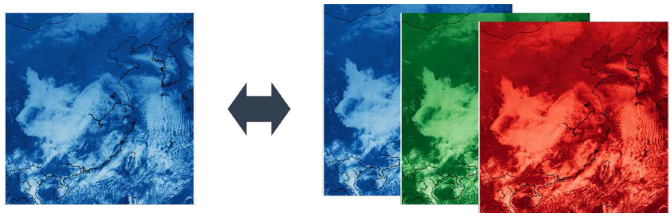

Fig. 4. Example of a paired dataset at the blue band and RGB bands of the AMI on Jan. 1, 2020, 03:40 UTC.

TABLE II
PAIRS OF INPUT AND OUTPUT DATA FOR MODEL CONSTRUCTION AND APPLICATION

Purpose/ Sensors	Input (X_O)	Input (Y_O)	Output (Y_V)
Construction/ AMI	Blue	Blue, Green, Red	Blue, Green, Red
Application/ GEMS	Blue	-	Blue, Green, Red

The reconstruction loss (L_1) plays a role in minimizing the distance between the hypothetical output dataset (Y'_V) and the observed output dataset (Y'_O) to reduce the blurry effects [61], which was calculated as follows [57]:

$$L_1(G) = E\left(\|Y'_O - Y'_V\|_1\right). \tag{7}$$

This research designated the AMI blue band data as X_O, while the combinations of AMI blue, green, and red bands data were utilized as Y_O. It is worth noting that we assumed the GEMS blue band to be similar to the AMI blue band, which led to the generation of virtual GEMS RGB bands using the D2D model.

Fig. 4 illustrates the concept of our D2D model development using the AMI blue band with dimensions of (1850 × 1900 × 1) as input data to produce virtual output data (RGB bands) with dimensions of (1850 × 1900 × 3) for training the D2D model. Table II summarizes the band pairs used for adversarial learning in the D2D model.

C. D2D Model Training and Test

This research utilized the preprocessed datasets of X_O and Y_O. X_O represents the AMI blue band radiance data, which has a size of (1850 × 1900 × 1), while Y_O is a (1850 × 1900 × 3) array created by stacking the AMI RGB bands radiance data.

During the training process, our D2D model was designed to simulate the generated virtual AMI RGB radiance data through the D2D translation and differentiate it from the observed AMI RGB radiance data. The D2D model experienced iterative training, and the iteration step was chosen to achieve the best possible values for CC and RMSE between the observed and D2D-generated AMI RGB radiance data. The constructed D2D

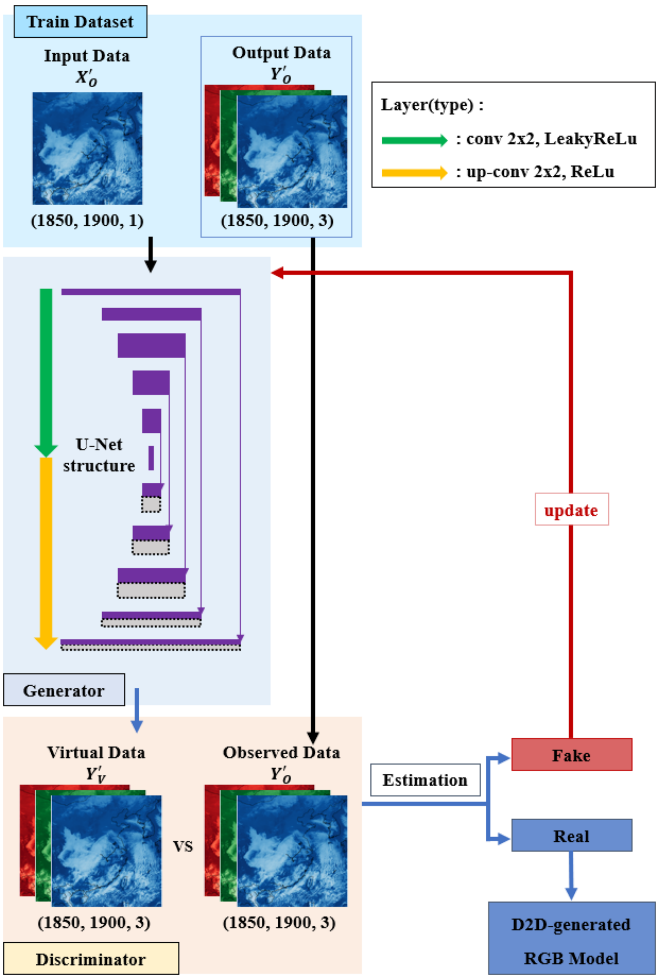

Fig. 5. Structure of the D2D model with generator (G) and discriminator (D).

model was tested using other input AMI blue band datasets not used during the model training processes. Remarkably, the D2D model exhibited an impressive ability to convert the AMI blue band data into quantitative AMI RGB data.

This research utilized the AMI datasets consisting of 703 pairs of data captured at 03:40 and 04:40 UTC from Jan. 01, 2020, to Dec. 31, 2020, for training the D2D model. Additionally, 72 pairs of AMI data were used for testing the D2D model, which were captured at 03:40 and 04:40 UTC on the 1st, 11th, and 21st day of every month between Jan. and Dec. 2021.

D. Virtual GEMS RGB Data Generation Using D2D Model

The constructed D2D model generates the virtual GEMS RGB bands radiance data using the observed GEMS blue band radiance data as the input dataset in the following manner:

$$Y_V = \text{GEMS}_{V,\text{RGB}} = \text{D2D model}\,(\text{GEMS}_{O,\text{Blue}}) \tag{8}$$

where $\text{GEMS}_{V,\text{RGB}}$ are the D2D-generated virtual GEMS RGB bands radiance data and $\text{GEMS}_{O,\text{Blue}}$ are the observed GEMS blue band radiance data.

Fig. 5 illustrates the D2D structure utilized in this research. The green- and yellow-colored arrows indicate the different operational layer types of each layer, whereas the purple boxes indicate feature maps and the grey boxes represent copied feature maps.

TABLE III
D2D MODEL PERFORMANCE CRITERIA

Performance	|rRMSE|	|rMBE|
Excellent	< 5 %	< 2 %
Good	5 to 10 %	2 to 5 %
Average	10 to 15 %	5 to 10 %
Poor	≥ 15 %	≥ 10 %

To apply the model, 71 pairs of GEMS blue band data were utilized at 03:45 and 04:45 UTC on the 1st, 11th, and 21st day of every month between Jan. and Dec. 2021. Notably, due to the missing GEMS data on May 11, 2021, at 06:45 UTC, 71 datasets of the GEMS were used for applying the constructed D2D model.

Our D2D model was implemented on a system consisting of an Intel Xeon CPU and two NVIDIA Titan-RTX GPUs, utilizing TensorFlow with Python 3.7.4 on a Linux Ubuntu 18.04.5 operating system with CUDA 10.0 and cuDNN 8.0.5.

E. Statistical Comparison

This research performed a statistical analysis between the D2D-generated results and the observed AMI RGB bands, using five indicators. Among them, CC, RMSE, and bias values were expressed as [62]

$$\text{CC} = \frac{\sum_{i=1}^{n}\left(Y_{V,i} - \overline{Y_V}\right)\sum_{i=1}^{n}\left(Y_{O,i} - \overline{Y_O}\right)}{\sqrt{\sum_{i=1}^{n}\left(Y_{V,i} - \overline{Y_V}\right)^2}\sqrt{\sum_{i=1}^{n}\left(Y_{O,i} - \overline{Y_O}\right)^2}} \tag{9}$$

$$\text{RMSE} = \sqrt{\sum_{i=1}^{n}\left(Y_{V,i} - Y_{O,i}\right)^2/n} \tag{10}$$

$$\text{Bias} = \sum_{i=1}^{n}\left(Y_{V,i} - Y_{O,i}\right)/n \tag{11}$$

where n denotes the total number of pixels in the AMI and GEMS data, i represents the index ranging from 1 to n, $Y_{O,i}$ is the ith pixel radiance data in the observed AMI data, and $Y_{V,i}$ means the virtual radiance of the ith pixel in the D2D-generated AMI and GEMS data. Moreover, $\overline{Y_O}$ and $\overline{Y_V}$ correspond to the averaged radiance values of the observed and D2D-generated data. Two additional indicators, relative RMSE (rRMSE) and relative mean bias error (rMBE) values, can show the D2D model performance criteria [62], which are classified as excellent, good, average, and poor. Table III summarizes the D2D model performance criteria

$$\text{rRMSE} = \text{RMSE}/\,\overline{Y_O} \tag{12}$$

$$\text{rMBE} = \text{Bias}/\,\overline{Y_O}. \tag{13}$$

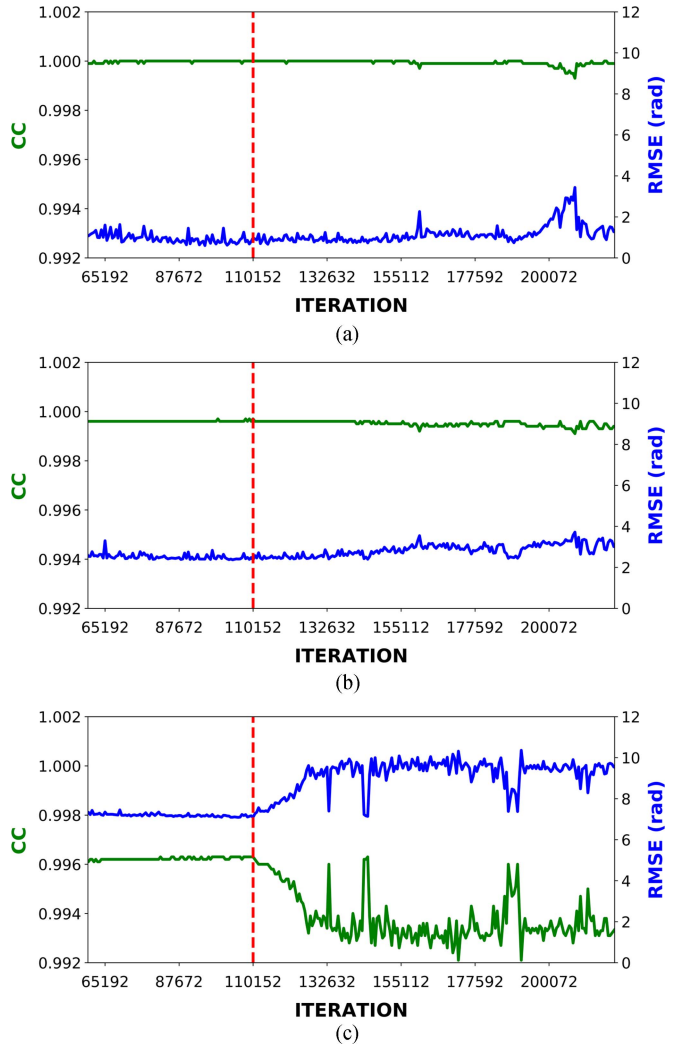

Fig. 6. CC and RMSE changes during model training iterations at (a) blue, (b) green, and (c) red bands between the observed and D2D-generated AMI on Jan. 1, 2021, at 03:40 UTC.

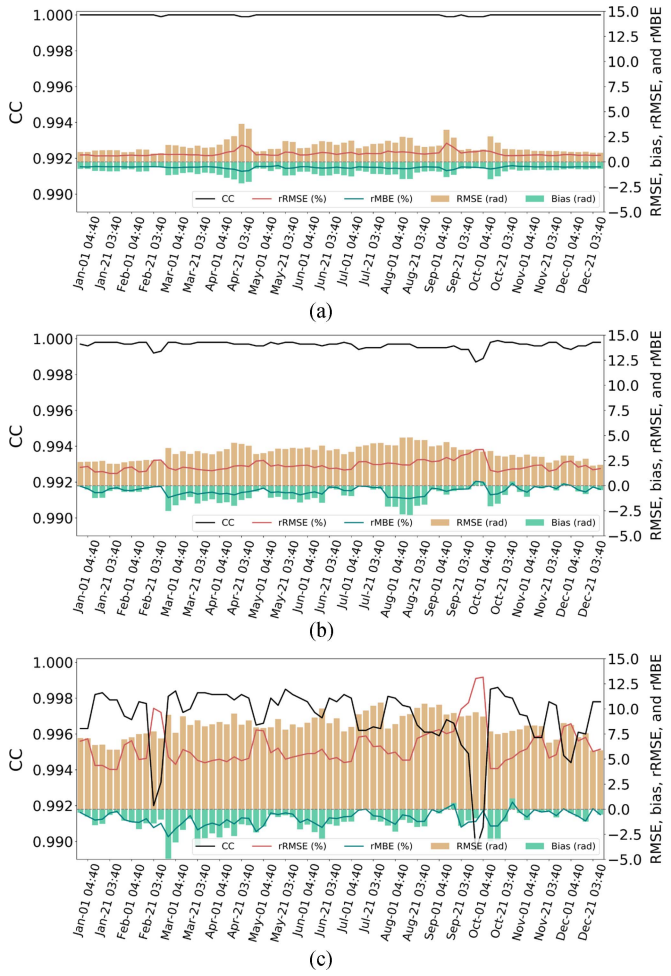

Fig. 7. Changes in CC, RMSE, bias, rRMSE, and rMBE for test cases at (a) blue, (b) green, and (c) red bands between the observed and D2D-generated AMI.

IV. Results

A. Advanced Meteorological Imager

Fig. 6 displays the changes in CC and RMSE values of the observed and D2D-generated AMI RGB band radiance data during the model training iterations. This research adopted the optimum model corresponding to iteration 110 152 as the D2D model. At 03:40 UTC on Jan. 1, 2021, the adopted D2D model demonstrated the CC and RMSE with 1 and 0.977 rad for the blue band; 0.999 and 2.360 rad for the green band; 0.996 and 7.087 rad for the red band, respectively.

Fig. 7 depicts the variations in CC, RMSE, bias, rRMSE, and rMBE of test cases for the RGB bands of the observed and D2D-generated AMI. The quantitative statistical results in the blue and green bands show better performance than those in the red band. Table IV presents a summary of the accuracy of the developed D2D model, indicating outstanding values of CC, RMSE, bias, rRMSE, and rMBE between the observed and D2D-generated AMI RGB bands. The rMBE and rRMSE, which are the model performance assessment criteria, showed excellent performance except for the red band's rRMSE, which showed good performance.

TABLE IV
Averaged Statistical Results for Test Cases Comparing the Observed and D2D-Generated AMI RGB Bands

Bands	Blue	Green	Red
CC	1.000	1.000	0.997
RMSE (rad)	1.551	3.314	8.337
Bias (rad)	-1.057	-0.928	-1.291
rRMSE (%)	0.816	1.991	6.264
rMBE (%)	0.553	0.491	0.886

Fig. 8(a) and (b) shows the true-color RGB images for one of the validation datasets of the AMI data with the observed and D2D-generated AMI on Feb. 21, 2021, 03:40 UTC. The D2D-generated AMI RGB bands exhibited qualitative accuracy. Fig. 8(c), (d), and (e) shows the spatial differences between the observed and D2D-generated AMI RGB bands. The differences of the blue and green bands radiance data were smaller than those in the red band due to the different spectral responses in each band. The D2D-generated AMI red band underestimated

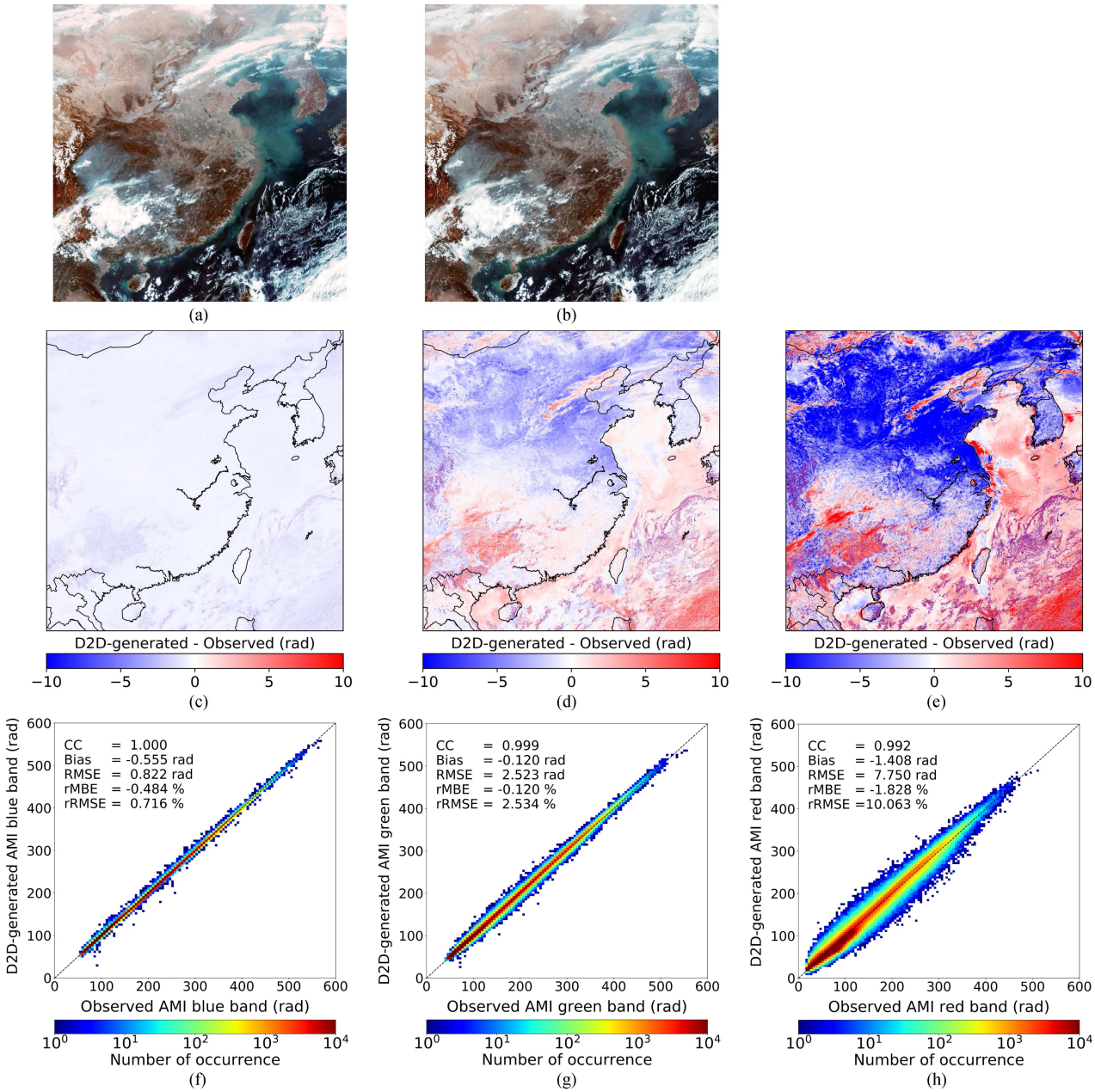

Fig. 8. (a) Observed and (b) D2D-generated AMI RGB images; spatial differences between the observed and D2D-generated AMI at the (c) blue, (d) green, and (e) red bands in radiance ranging from −10 to 10; scatterplots between the observed and D2D-generated AMI at the (f) blue, (g) green, and (h) red bands. The time was 03:40 UTC on Feb. 21, 2021.

the radiance values in a part of inland China, whereas it partially overestimated the radiance values in the clouds. Fig. 8(f), (g), and (h) displays the scatterplots between the observed and D2D-generated AMI RGB bands with CC = 1.000, RMSE = 0.822 rad, bias = −0.555 rad, rRMSE = 0.716%, and rMBE = −0.484% for the blue band; CC = 0.999, RMSE = 2.523 rad, bias = −0.120 rad, rRMSE = 2.534%, and rMBE = −0.120% for the green band; and CC = 0.992, RMSE = 7.750 rad, bias = −1.408 rad, rRMSE = 10.063%, and rMBE = −1.828% for the red band.

The obtained results suggest that the proposed D2D model exhibits remarkable accuracy. Notably, the blue and green bands exhibit similar accuracy, while the red band shows relatively lower accuracy due to its wider spectral bandwidth compared to the other visible bands, as well as the spectral difference between blue and red bands.

B. Geostationary Environment Monitoring Spectrometer

Fig. 9 shows the changes in statistical results for application cases at the blue band between the observed and D2D-generated GEMS. Table V indicates the averaged values with CC = 0.999, RMSE = 3.450 rad, bias = −1.858 rad, rRMSE = 1.559%, and rMBE = 0.847%.

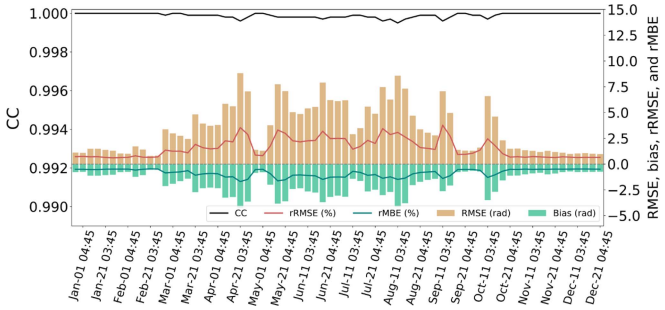

Fig. 9. Changes in CC, RMSE, bias, rRMSE, and rMBE for application cases at the blue band between the observed and D2D-generated GEMS.

TABLE V
AVERAGED STATISTICAL RESULTS FOR APPLICATION CASES COMPARING THE OBSERVED AND D2D-GENERATED GEMS BLUE BAND

Band	CC	RMSE (W/cm²/cm/sr)	Bias (W/cm²/cm/sr)	rRMSE (%)	rMBE (%)
Blue	0.999	3.450	-1.858	1.559	0.847

TABLE VI
AVERAGED STATISTICAL RESULTS FOR APPLICATION CASES COMPARING THE OBSERVED AMI AND THE D2D-GENERATED GEMS RGB BANDS

Bands	Blue	Green	Red
CC	0.926	0.924	0.913
RMSE (rad)	51.010	50.236	48.812
Bias (rad)	15.630	14.831	12.843

Fig. 10(a) shows the scatterplot between the observed and D2D-generated GEMS blue band on Feb. 21, 2021, at 03:45 UTC. In terms of radiance, the CC, RMSE, bias, rRMSE, and rMBE comparing the two data were 1.000, 0.794 rad, −0.560 rad, 0.651%, and −0.459%, respectively. These results appear to be similar to those of the AMI blue band comparison. Furthermore, Fig. 10(b) shows good agreement in the spatial difference between the observed and D2D-generated GEMS blue band. However, the D2D-generated GEMS blue band showed a slight underestimation of high radiance values, which was observed in the cloud area.

Fig. 11 shows the changes in quantitative statistical results for application cases at the RGB bands between the observed AMI and the D2D-generated GEMS. Since there was a 5-min difference in the observation time between the AMI and GEMS, the accuracy was relatively low compared to the AMI test cases. Similar to the AMI test results, the accuracy of the blue and green bands in the GEMS application results were relatively better than that of the red band. Table VI indicates the averaged statistical values comparing the observed AMI and the D2D-generated GEMS RGB bands. Regarding the radiance range, the D2D-generated GEMS exhibit the averaged uncertainties of approximately 6.624%, 7.142%, and 7.697% for the blue, green, and red bands, respectively, despite the 5-min observation time difference with the AMI.

Fig. 12(a) shows the observed AMI true-color RGB image on Feb. 21, 2021, at 03:40 UTC, and Fig. 12(b) shows the D2D-generated GEMS true-color RGB images on Feb. 21, 2021, at 03:45 UTC using the D2D-generated GEMS RGB bands.

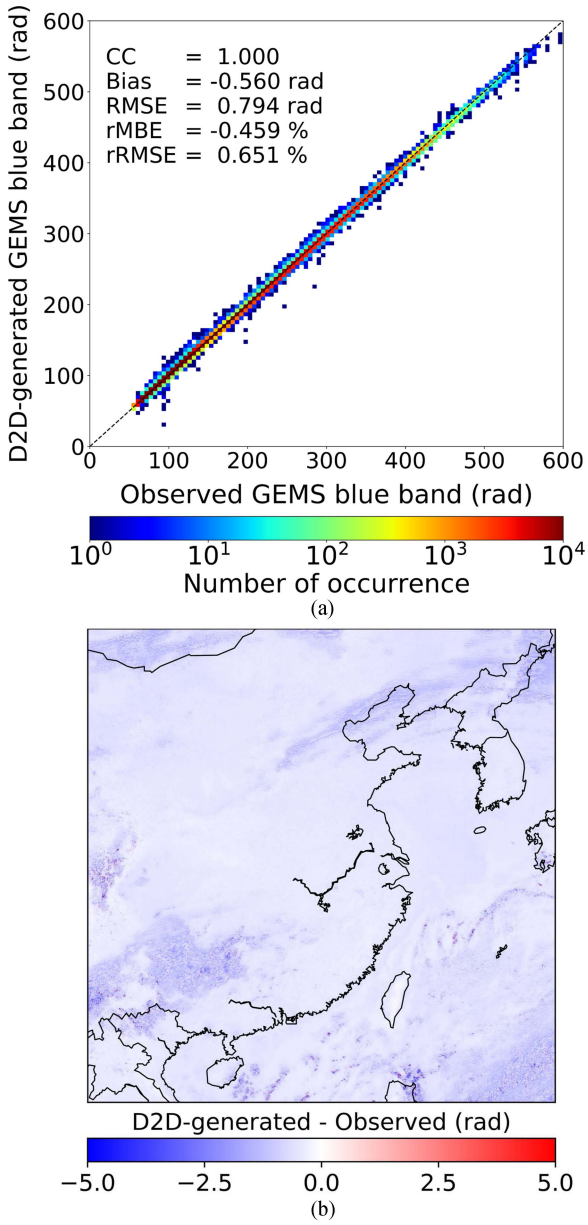

Fig. 10. (a) Scatterplot and (b) spatial difference between the observed and D2D-generated GEMS blue band. The time was Feb. 21, 2021, at 03:45 UTC.

Notably, there was a 5-min difference in the observation time between the AMI and GEMS. The D2D-generated GEMS RGB image was qualitatively accurate and was similar to the observed AMI RGB image. Fig. 12(c), (d), and (e) shows the spatial differences between the AMI and GEMS in the RGB bands. There are relatively large variances in the cloudy pixels owing to the 5-min time difference between the AMI and GEMS observations. Nevertheless, these outcomes exhibit a superior level of precision and minimal error in the D2D-generated GEMS RGB bands as compared to the observed AMI RGB band. Fig. 12(f), (g), and (h) shows the scatterplots between the observed AMI and the D2D-generated GEMS at the RGB bands. The CC, RMSE, and bias values between the observed AMI and the D2D-generated GEMS data were 0.920, 27.803 rad, and

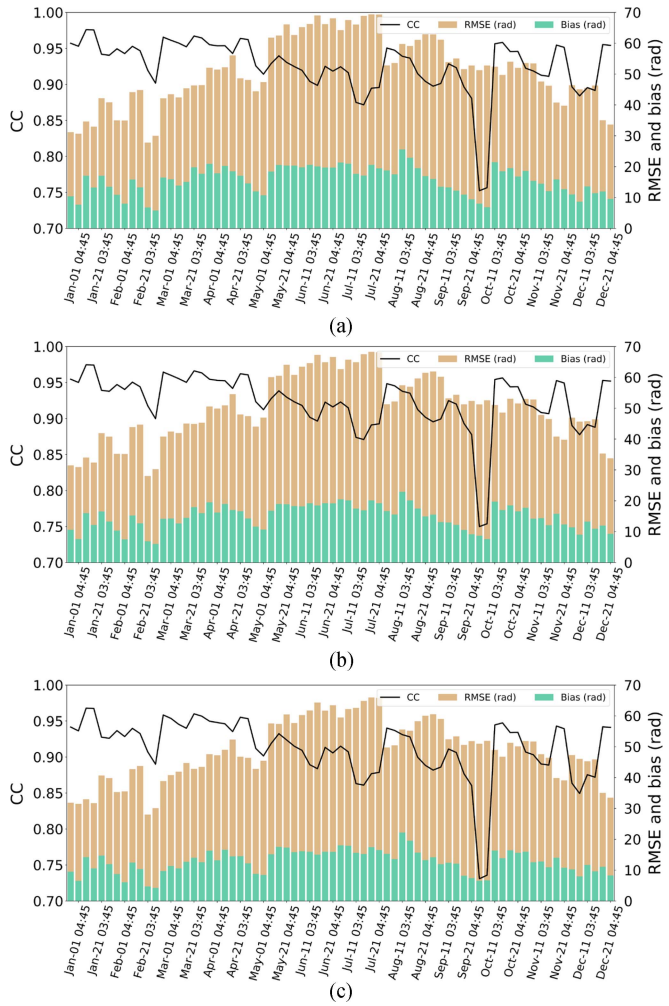

Fig. 11. Changes in CC, RMSE, and bias for application cases at the (a) blue, (b) green, and (c) red bands between the observed AMI and the D2D-generated GEMS.

6.776 rad in the blue band; 0.918, 28.065 rad, and 6.908 rad in the green band; and 0.907, 28.028 rad, and 4.671 rad in the red band, respectively.

Despite the 5-min time difference, the D2D-generated GEMS RGB band data matched the observed AMI RGB band data with consistent accuracy (see Fig. 3). The D2D-generated GEMS red band has a similar accuracy to the D2D-generated GEMS blue and green bands compared to the results of the D2D-generated AMI data. The D2D-generated GEMS RGB bands overestimated the cloud pixels because of the rapid movement of clouds within five minutes of the two sensors' observation time difference. In contrast, the D2D-generated GEMS demonstrated comparable or reduced radiance values at cloud-free pixels and followed a similar pattern to the D2D-generated AMI RGB bands.

V. Discussion

This research presented a D2D-driven approach to simulate the virtual green and red bands of the GEMS with a blue band, based on the assumption that the DL model constructed using the AMI observed RGB bands can produce the radiances of virtual GEMS blue, green, and red bands. This research represents a significant contribution to the field of satellite remote sensing, as it enables the simulation of physically meaningful information for nonexistent observations of a satellite using deep-learning techniques, in contrast to previous researches dealing with image-to-image translation.

In previous research [48], the generation of virtual green bands in an ABI sensor was investigated using an analogous AHI sensor with similar SRFs to the ABI sensor. However, the research encountered errors and limitations due to different solar effects caused by the different locations of the two sensors. In another research [55], hypothetical nighttime AMI RGB bands were developed using the pairs of VIS and IR bands of the same sensor and location. Nevertheless, this approach had limitations in assuming consistent IR bands during day and night, making it unsuitable for regions with high daily variation in surface temperature, such as desert areas. In contrast to the previous research, this research used two different sensors at the exact location.

This research has a limitation in that it relies on the highly correlated bands of the GEMS and the adjacent AMI, which possess similar VIS bands.

Another limitation of this research is caused by the differences between the AMI and GEMS. First, the approximately five-minute observation time difference led to different solar-sensor geometries between the AMI and GEMS. In addition, the two sensors captured different cloud locations and shapes, as shown in Fig. 12(c), (d), and (e). As a result, the D2D-generated GEMS RGB bands caused the overestimation of clouds and underestimation at the edges of clouds. Second, the GEMS and AMI blue bands have the same central wavelength of 470 nm but different bandwidths. Hence, the two sensors observed different amounts of energy reflected from Earth, as shown in Fig. 3. The difference in the SRFs between the AMI and GEMS blue bands resulted in the overestimation of cloud pixels in the observed GEMS blue band (see Fig. 3).

The degraded results of the D2D models may be related to various noise effects and spectral variabilities between the GEMS and AMI, resulting in different land, sea, and cloud responses, as presented in Figs. 8 and 12. For instance, the D2D-generated GEMS blue and green bands overestimate surface reflectance in land, sea, and cloud in Fig. 12, while the D2D-generated AMI blue and green bands underestimate land and stratiform cloud in Fig. 8. It is worth noting that only radiances were used as input data in this research. Thus, incorporating additional physical variables such as surface albedo and clear-sky reflectance based on rigorous radiative transfer calculation for training the D2D model in future work could improve the over- and underestimation produced in the proposed D2D model and yield more accurate and reliable results.

This study encountered another limitation by utilizing the AMI and GEMS data at a specific time, neglecting the temporal variation of solar effects. Future research to enhance the applicability of the developed D2D model throughout the

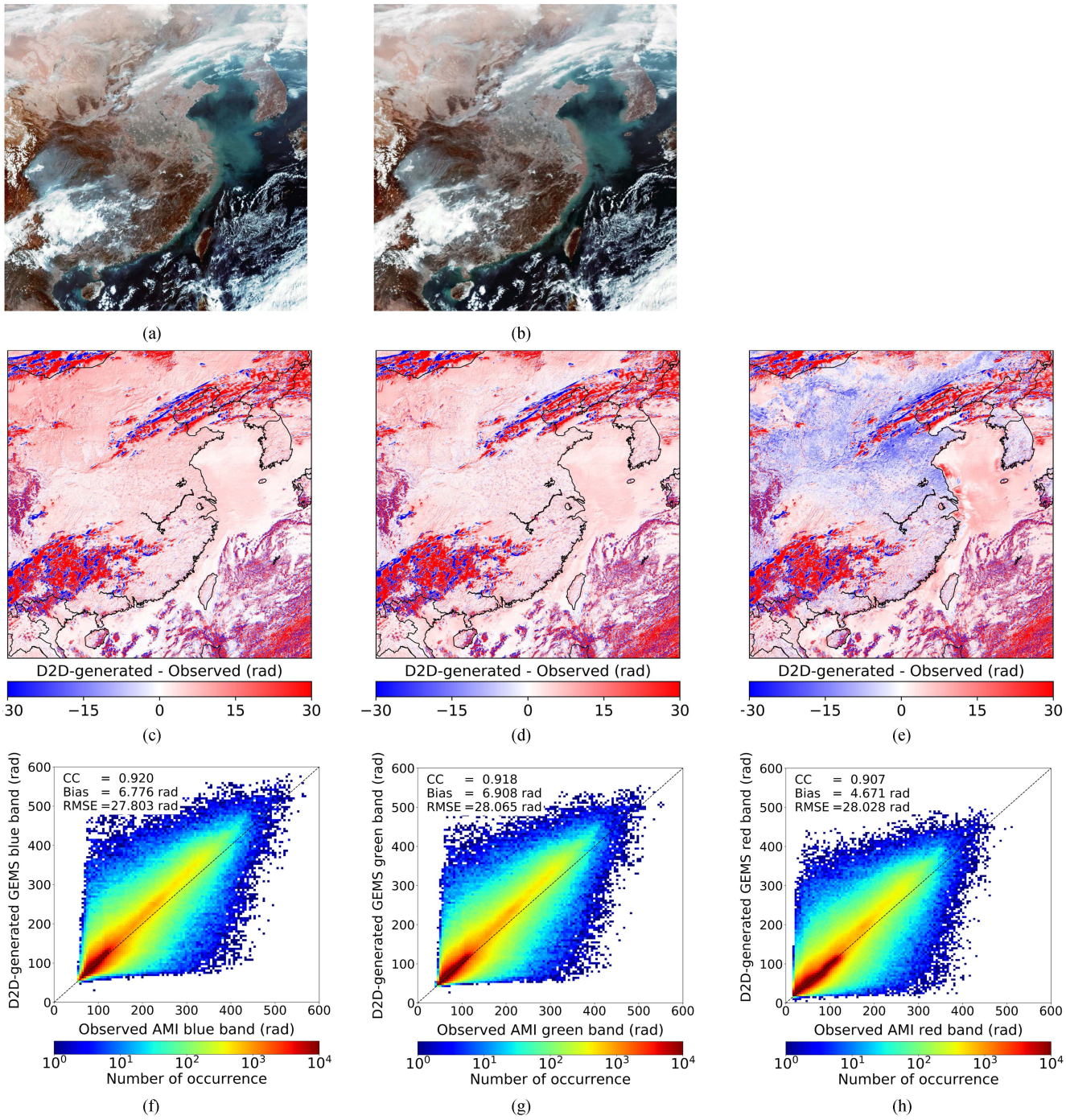

Fig. 12. (a) Observed AMI RGB (03:40 UTC) and (b) D2D-generated GEMS RGB images (03:45 UTC); Spatial differences between the observed AMI and the D2D-generated GEMS at the (c) blue, (d) green, and (e) red bands in radiance from −30 to 30, scatterplots between the observed AMI and the D2D-generated GEMS at the (f) blue, (g) green, and (h) red bands. The time difference between the two sensors was 5 min. The date was Feb. 21, 2021.

entire daytime will include a data processing procedure that mitigates the influence of solar effects. One potential approach involves normalizing the AMI and GEMS data using the cosine of the solar zenith angle to mitigate the dependency on temporal variations in radiance levels.

An additional limitation of this research was the computational demand required to generate high-resolution full-disk data using the DL model, which was memory-intensive on GPUs despite rapid advancements in hardware performance.

In this study, the absence of a normalization process could converge to local optima during the D2D model training process for simulating AMI and GEMS data due to the differences and discrepancies in the spectral range of the AMI and GEMS sensors. A denormalization process in the D2D model enabled the restoration of the virtual results to the radiance ranges of AMI and GEMS observations. Additionally, a GAN-based DL approach, among other DL methods, was fit to generate virtual GEMS green and red bands. The quantitative validation of the

D2D model was infeasible without the availability of overlapping observation data between AMI and GEMS. Nevertheless, the use of ResNet instead of the UNet in the generator, different normalization and denormalization, and various types of GANs may impact the results of this study.

Despite these limitations, this research still offers the valuable capability of generating nonexistent RGB bands for an existing GEMS. It produced virtual RGB band observation data, which was impossible using the current GEMS and traditional approaches to satellite remote sensing. The presented D2D method can support global atmospheric environment monitoring and estimate the movement and distribution of AOD and dust in Asia. As a potential future research to enhance the proposed D2D model for virtual GEMS RGB generation, advanced DL models will be explored, including a fusion of DL methods [63], diverse fusion and training strategies using a multimodal DL framework [64], and integration of the u-net in u-net architecture [65] within the D2D model.

VI. Summary and Conclusions

Geostationary satellites equipped with UV and VIS sensors have been instrumental in monitoring the global atmospheric environment and tracing the transportation of atmospheric chemical compositions. The GEMS, onboard the GK-2B satellite, is the first next-generation atmospheric environmental sensor on GEO satellites that monitors the atmospheric environment spatiotemporally, including aerosols, clouds, O_3, NO_2, SO_2, HCHO, surface reflectivity, and UVI information. However, GEMS lacks green and red bands in its VIS spectrum, which are helpful in understanding and visualizing diverse surface and atmospheric information for both specialists and nonexperts.

This research presents a novel method for generating virtual GEMS green and red bands radiance data using DL techniques with paired datasets of the AMI RGB bands. The proposed DL model was trained using pairs of the AMI blue band and AMI RGB bands through an adversarial DL method with the Pix2Pix program implemented on Linux-based operating systems, utilizing two NVIDIA Titan-RTX GPUs and an Intel Xeon CPU. The radiance data of the D2D-generated AMI green and red bands exhibited a remarkable statistical agreement with the observed AMI green and red bands radiance data. Based on the validation results, the D2D model was employed to generate the nonexistent GEMS green and red bands radiance data. The observed AMI RGB bands and the D2D-generated GEMS RGB bands were compared and showed excellent agreement, with high CC, low RMSE, and bias values.

As future research, the methodology presented in this research can be extended to generate missing VIS bands in polar orbit satellites for monitoring atmospheric environments, such as the TROPOMI sensor aboard the Sentinel-5 Precursor satellite. The TROPOMI sensor covers UV and VIS (270–495 nm), near-infrared (710–775 nm), and short-wave infrared (2305–2385 nm) bands. Moreover, the D2D methodology may be relevant to other geostationary atmospheric environment satellites lacking VIS bands. For instance, NASA's Tropospheric Emissions Monitoring of Pollution (TEMPO), launched on Apr. 7, 2023, has UV and VIS spectrometers. Similarly, the ESA's Sentinel-4 satellite, equipped with an ultraviolet-visible near-infrared imaging spectrometer (UVN) covering the UV (305–400 nm), VIS (400–500 nm), and near-infrared (750–775 nm) bands, will be launched in 2024.

The D2D method detailed in this research can potentially produce in situ virtual RGB images of TROPOMI, OMI, TEMPO, and UVN instruments for monitoring atmospheric environments. Such capability could enhance our understanding and management of air quality, climate change, and other environmental issues.

Conflict of Interest

The authors declare no competing financial interest.

Acknowledgment

The authors would like to thank anonymous reviewers for helpful and constructive comments on the manuscript.

References

[1] M. Brauer et al., "Ambient air pollution exposure estimation for the global burden of disease 2013," *Environ. Sci. Technol.*, vol. 50, no. 1, pp. 79–88, 2016.

[2] A. J. Cohen et al., "Estimates and 25-year trends of the global burden of disease attributable to ambient air pollution: An analysis of data from the global burden of diseases study 2015," *Lancet*, vol. 389, no. 10082, pp. 1907–1918, 2017.

[3] J. Kim et al., "New era of air quality monitoring from space: Geostationary environment monitoring spectrometer (GEMS)," *Bull. Amer. Meteorological Soc.*, vol. 101, no. 1, pp. E1–E22, 2020.

[4] P. F. Levelt et al., "The ozone monitoring instrument: Overview of 14 years in space," *Atmospheric Chem. Phys.*, vol. 18, no. 8, pp. 5699–5745, 2018.

[5] J. P. Burrows et al., "The global ozone monitoring experiment (GOME): Mission concept and first scientific results," *J. Atmospheric Sci.*, vol. 56, no. 2, pp. 151–175, 1999.

[6] A. E Space et al., *GOME : Global Ozone Monitoring Experiment : Interim Science Report*. Noordwijk, The Netherlands: European Space Agency, 1993.

[7] R. Munro et al., "The GOME-2 instrument on the Metop series of satellites: Instrument design, calibration, and level 1 data processing–an overview," *Atmospheric Meas. Techn.*, vol. 9, no. 3, pp. 1279–1301, 2016.

[8] R. Levy et al., "The collection 6 MODIS aerosol products over land and ocean," *Atmospheric Meas. Techn.*, vol. 6, no. 11, pp. 2989–3034, 2013.

[9] L. Flynn et al., "Performance of the ozone mapping and profiler suite (OMPS) products," *J. Geophysical Res., Atmospheres*, vol. 119, no. 10, pp. 6181–6195, 2014.

[10] H. Bovensmann et al., "SCIAMACHY: Mission objectives and measurement modes," *J. Atmospheric Sci.*, vol. 56, no. 2, pp. 127–150, 1999.

[11] D. Heath et al., "The solar backscatter ultraviolet and total ozone mapping spectrometer (SBUV/TOMS) for Nimbus G," *Opt. Eng.*, vol. 14, no. 4, 1975, Art. no. 144323.

[12] J. Veefkind et al., "TROPOMI on the ESA sentinel-5 precursor: A GMES mission for global observations of the atmospheric composition for climate, air quality and ozone layer applications," *Remote Sens. Environ.*, vol. 120, pp. 70–83, 2012.

[13] J. M. Jackson et al., "Suomi-NPP VIIRS aerosol algorithms and data products," *J. Geophysical Res., Atmospheres*, vol. 118, no. 22, pp. 12673–12689, 2013.

[14] S. Go et al., "Synergistic use of hyperspectral UV-visible OMI and broadband meteorological imager MODIS data for a merged aerosol product," *Remote Sens.*, vol. 12, no. 23, 2020, Art. no. 3987.

[15] H.-A. Kwon et al., "Description of a formaldehyde retrieval algorithm for the geostationary environment monitoring spectrometer (GEMS)," *Atmospheric Meas. Techn.*, vol. 12, no. 7, pp. 3551–3571, 2019.

[16] J. Lasnik et al., "Geostationary environment monitoring spectrometer (GEMS) over the Korea Peninsula and Asia-pacific region," *AGU Fall Meeting Abstr.*, pp. A51A–3003, Dec. 2014.

[17] U. Jeong et al., "An optimal-estimation-based aerosol retrieval algorithm using OMI near-UV observations," *Atmospheric Chem. Phys.*, vol. 16, no. 1, pp. 177–193, 2016.

[18] S. S. Park et al., "Utilization of O4 slant column density to derive aerosol layer height from a spaceborne UV-Visible hyperspectral sensor: Sensitivity and case study," *Atmos. Chem. Phys.*, vol. 16, no. 4, pp. 1987–2006, Feb., 2016.

[19] O. Torres, C. Ahn, and Z. Chen, "Improvements to the OMI near-UV aerosol algorithm using A-train CALIOP and AIRS observations," *Atmospheric Meas. Techn.*, vol. 6, no. 11, pp. 3257–3270, 2013.

[20] M. Kim et al., "Optimal estimation-based algorithm to retrieve aerosol optical properties for GEMS measurements over Asia," *Remote Sens.*, vol. 10, no. 2, 2018, Art. no. 162.

[21] P. Stammes et al., "Effective cloud fractions from the ozone monitoring instrument: Theoretical framework and validation," *J. Geophysical Res., Atmospheres*, vol. 113, no. D16, 2008, Art. no. 254102.

[22] D. P. Haffner et al., "The TOMS v9 algorithm for OMPS nadir mapper total ozone: An enhanced design that ensures data continuity," *AGU Fall Meeting Abstr.*, pp. A51A–3003, Dec. 2015.

[23] K. Baek et al., "Evaluation of total ozone measurements from geostationary environmental monitoring satellite (GEMS)," *EGUsphere*, vol. 9, pp. 1–23, 2022.

[24] H. Hong et al., "The effects of aerosol on the retrieval accuracy of NO2 slant column density," *Remote Sens.*, vol. 9, no. 8, 2017, Art. no. 867.

[25] P. Junsung, *Development of the Geostationary Environment Monitoring Spectrometer (GEMS) NO2 Retrieval Algorithm and First-time Observations of Its Diurnal Characteristics over Asia*. Busan, South Korea: Pukyong National University, 2022.

[26] C. Li et al., "A fast and sensitive new satellite SO2 retrieval algorithm based on principal component analysis: Application to the ozone monitoring instrument," *Geophysical Res. Lett.*, vol. 40, no. 23, pp. 6314–6318, 2013.

[27] C. C Miller et al., "Glyoxal retrieval from the ozone monitoring instrument," *Atmospheric Meas. Techn.*, vol. 7, no. 11, pp. 3891–3907, 2014.

[28] K. Chance et al., "Satellite observations of formaldehyde over north America from GOME," *Geophysical Res. Lett.*, vol. 27, no. 21, pp. 3461–3464, 2000.

[29] G. González Abadr et al., "Smithsonian astrophysical observatory ozone mapping and profiler suite (SAO OMPS) formaldehyde retrieval," *Atmospheric Meas. Techn.*, vol. 9, no. 7, pp. 2797–2812, 2016.

[30] K. Lee and J. Yoo, "Determination of directional surface reflectance from geostationary satellite observations," *SPIE Asia-Pacific Remote Sens.*, vol. 31, pp. 10777–10752, 2018.

[31] H. Lee et al., "Preliminary results of UV index and other biological indices in Asia for the geostationary environmental monitoring spectrometer (GEMS)," *Atmospheric Comp. Struct.*, vol. 345, pp. A003–0007, 2020.

[32] J. - G. Lee et al., "Deep learning in medical imaging: General overview," *Korean J. Radiol.*, vol. 18, no. 4, pp. 570–584, 2017.

[33] X. - W. Chen and X. Lin, "Big data deep learning: Challenges and perspectives," *IEEE Access*, vol. 2, pp. 514–525, 2014.

[34] Y. Tao et al., "A two-stage deep neural network framework for precipitation estimation from bispectral satellite information," *J. Hydrometeorology*, vol. 19, no. 2, pp. 393–408, 2018.

[35] X. Shi et al., "Convolutional LSTM network: A machine learning approach for precipitation nowcasting," *Adv. Neural Inf. Process. Syst.*, vol. 28, 2015, Art. No. 251025.

[36] C. Chen, X. Chen, and H. Cheng, "On the over-smoothing problem of CNN based disparity estimation," in *Proc. IEEE/CVF Int. Conf. Comput. Vis.*, 2019, pp. 8997–9005.

[37] H.-H. Xu and D.-Y. Ge, "A novel image edge smoothing method based on convolutional neural network," *Int. J. Adv. Robot. Syst.*, vol. 17, no. 3, 2020, Art. no. 1729881420921676.

[38] E. L. Denton, S. Chintala, and R. Fergus, "Deep generative image models using a laplacian pyramid of adversarial networks," *Adv. Neural Inf. Process. Syst.*, vol. 28, 2015, Art. no. 25421.

[39] T. Kim, M. Cha, H. Kim, J. K. Lee, and J. Kim, "Learning to discover cross-domain relations with generative adversarial networks," in *Proc. 34th Int. Conf. Mach. Learn.*, 2017, pp. 1857–1865.

[40] X. Mao et al., "Least squares generative adversarial networks," *Generative Adversarial Netw.*, vol. 9, pp. 2794–2802, 2019.

[41] A. Odena, C. Olah, and J. Shlens, "Conditional image synthesis with auxiliary classifier gans," in *Proc. 34th Int. Conf. Mach. Learn.*, 2017, pp. 2642–2651.

[42] A. Radford, L. Metz, and S. Chintala, "Unsupervised representation learning with deep convolutional generative adversarial networks," 2015. Accessed: Oct. 1, 2023. [Online]. Available: http://arxiv.org/abs/1511.06434

[43] C. N. d. Santos, K. Wadhawan, and B. Zhou, "Learning loss functions for semi-supervised learning via discriminative adversarial networks," 2017. Accessed: Oct. 1, 2023. [Online]. Available: https://arxiv.org/abs/1707.02198

[44] J. - Y. Zhu, T. Park, P. Isola, and A. A. Efros, "Unpaired image-to-image translation using cycle-consistent adversarial networks," in *Proc. IEEE Int. Conf. Comput. Vis.*, 2017, pp. 2223–2232.

[45] K. Kim et al., "Nighttime reflectance generation in the visible band of satellites," *Remote Sens.*, vol. 11, no. 18, 2019, Art. no. 2087.

[46] Y. Kim and S. Hong, "Deep learning-generated nighttime reflectance and daytime radiance of the midwave infrared band of a geostationary satellite," *Remote Sens.*, vol. 11, no. 22, 2019, Art. no. 2713.

[47] C. Li and M. Wand, "Precomputed real-time texture synthesis with Markovian generative adversarial networks," in *Proc. Eur. Conf. Comput. Vis.*, 2016, pp. 702–716.

[48] J.-E. Park, G. Kim, and S. Hong, "Green band generation for advanced baseline imager sensor using Pix2Pix with advanced baseline imager and advanced himawari imager observations," *IEEE Trans. Geosci. Remote Sens.*, vol. 59, no. 8, pp. 6415–6423, Aug. 2020.

[49] S. Park et al., "Estimation of ground-level particulate matter concentrations through the synergistic use of satellite observations and process-based models over South Korea," *Atmospheric Chem. Phys.*, vol. 19, no. 2, pp. 1097–1113, 2019.

[50] Y. Lee et al., "Spectral replacement using machine learning methods for continuous mapping of geostationary environment monitoring spectrometer (GEMS)," *Atmospheric Meas. Techn. Discuss.*, vol. 31, pp. 1–18, 2022.

[51] J.-M. Yeom, S. Jeong, J.-S. Ha, K.-H. Lee, C.-S. Lee, and S. Park, "Estimation of the hourly aerosol optical depth from GOCI geostationary satellite data: Deep neural network, machine learning, and physical models," *IEEE Trans. Geosci. Remote Sens.*, vol. 60, pp. 1–12, Sep. 2022, Art. no. 4103612.

[52] Y. Kim and S. Hong, "Convective cloud RGB product and its application to tropical cyclone analysis using geostationary satellite observation," *J. Korean Earth Sci. Soc.*, vol. 40, no. 4, pp. 406–413, 2019.

[53] I. Blanes, J. Serra-Sagrista, M. W. Marcellin, and J. Bartrina-Rapesta, "Divide-and-conquer strategies for hyperspectral image processing: A review of their benefits and advantages," *IEEE Signal Process. Mag.*, vol. 29, no. 3, pp. 71–81, May 2012.

[54] L. Remer et al., "Retrieving aerosol in a cloudy environment: Aerosol product availability as a function of spatial resolution," *Atmospheric Meas. Techn.*, vol. 5, no. 7, pp. 1823–1840, 2012.

[55] K.- H. Han, J.- C. Jang, S. Ryu, E.-H. Sohn, and S. Hong, "Hypothetical visible bands of advanced meteorological imager onboard the geostationary korea multi-purpose satellite-2A using data-to-data translation," *IEEE J. Sel. Topics Appl. Earth Observ. Remote Sens.*, vol. 15, pp. 8378–8388, Sep. 2022.

[56] P. Isola, J-Y. Zhu, T. Zhou, and A. A. Efros, "Image-to-image translation with conditional adversarial networks," in *Proc. IEEE Conf. Comput. Vis. Pattern Recognit.*, 2017, pp. 1125–1134.

[57] Y. Lin, "Pix2pix-tensorflow," *Github Repository.* 2016. [Online]. Available: https://github.com/yenchenlin/pix2pix-tensorflow

[58] M. Mirza and S. Osindero, "Conditional generative adversarial nets," 2014. Accessed: Oct. 1, 2023. [Online]. Available: http://arxiv.org/abs/1411.1784

[59] I. Goodfellow et al., "Generative adversarial nets," *Adv. Neural Inf. Process. Syst.*, vol. 27, 2014, Art. no. 25100.

[60] V. Nguyen, T. F. Y. Vicente, M. Zhao, M. Hoai, and D. Samaras, "Shadow detection with conditional generative adversarial networks," in *Proc. IEEE Int. Conf. Comput. Vis.*, 2017, pp. 4510–4518.

[61] D. Michelsanti and Z. - H. Tan, "Conditional generative adversarial networks for speech enhancement and noise-robust speaker verification," in *Proc. Interspeech*, Aug. 2017, pp. 2008–2012.

[62] N. Engerer and F. Mills, "Validating nine clear sky radiation models in Australia," *Sol. Energy*, vol. 120, pp. 9–24, 2015.

[63] D. Hong, L. Gao, J. Yao, B. Zhang, A. Plaza, and J. Chanussot, "Graph convolutional networks for hyperspectral image classification," *IEEE Trans. Geosci. Remote Sens.*, vol. 59, no. 7, pp. 5966–5978, Jul. 2021.

[64] D. Hong et al., "More diverse means better: Multimodal deep learning meets remote-sensing imagery classification," *IEEE Trans. Geosci. Remote Sens.*, vol. 59, no. 5, pp. 4340–4354, May 2021.

[65] X. Wu, D. Hong, and J. Chanussot, "UIU-Net: U-Net in U-net for infrared small object detection," *IEEE Trans. Image Process.*, vol. 32, pp. 364–376, Dec. 2022.

Han-Sol Ryu received the B.S. degree in environmental engineering in 2019 from Sejong University, Seoul, South Korea, where she is currently working toward the Integrated M.S. and Ph.D. degrees in environmental sciences.

More specific areas of focus include the development of physical and deep learning-based algorithms for tasks such as fog detection and forecasting, flood detection, and the simulation of missing bands in operating optical and microwave satellites. Her primary research interests include the applications of satellite remote sensing and deep learning methodologies to environmental studies.

Jeong-Eun Park received the B.S. degree in environmental engineering in 2019 from Sejong University, Seoul, South Korea, where she is currently working toward the Integrated M.S. and Ph.D. degrees in environmental sciences.

Her research interests include remote sensing and deep learning techniques in earth's environment.

Jaehoon Jeong received the Ph.D. degree in geoinformatics engineering from Inha University, Incheon, South Korea, in 2014.

He is currently a Senior Researcher with the Environmental Satellite Center, National Institute of Environmental Research, South Korea. His research interests include photogrammetric engineering and remote sensing data processing.

Sungwook Hong received the B.S. degree in earth science education and M.S. degree in physics from Seoul National University, Seoul, South Korea, in 1997 and 2000, respectively, and the M.S. and Ph.D. degrees in atmospheric sciences from Texas A&M University, College Station, TX, USA, in 2002 and 2006, respectively.

From 2006 to 2008, he was a Research Scientist with the National Oceanic and Atmospheric Administration. From 2008 to 2015, he was a Senior Research Scientist with the Korea Meteorological Administration. Since 2015, he has been an Associate Professor with the Department of Environment, Energy and Geoinformatics, Sejong University, Seoul, South Korea. He has authored of more than 80 articles, and more than 20 inventions. His research interests include satellite remote sensing algorithm developments based on physical methods and artificial intelligence techniques, as well as sensor development, and various atmospheric, oceanic, terrestrial, and environmental applications.